A Computational Model for Bipolar Deep Brain Stimulation of the Subthalamic Nucleus

Maria I. Iacono, Esra Neufeld, Giorgio Bonmassar, Esther Akinnagbe, Andras Jakab, Ethan Cohen, Niels Kuster, Wolfgang Kainz, Leonardo M. Angelone

Abstract— **Deep brain stimulation (DBS) of the subthalamic nucleus (STN) has been shown to reduce some of the symptoms of advanced, levodopa-responsive Parkinson's disease that are not adequately controlled with medication. However, the precise mechanism of the therapeutic action of DBS is still unclear. Stimulation-induced side effects are not uncommon and require electrical "dose" adjustments. Quantitative methods are needed to fully characterize the electric field in the deep brain region that surrounds the electrodes in order to help with adjustments and maximize the efficacy of the device.**

Herein we report a magnetic resonance imaging (MRI)-based head model proposed for analysis of fields generated by deep brain stimulation (DBS). The model was derived from multimodal image data at 0.5mm isotropic spatial resolution and distinguishes 142 anatomical structures, including the basal ganglia and 38 nuclei of the thalamus. Six bipolar electrode configurations (1-2, 1-3, 1-4, 2-3, 2-4, 3-4) were modeled in order to assess the effects of the inter-electrode distance of the electric field. Increasing the distance between the electrodes results in an attenuated stimulation, with up to 25% reduction in electric field amplitude delivered (2-3 vs. 1-4). The map of the deep brain structures provided a highly precise anatomical detail which is useful for the quantitative assessment of current spread around the electrode and a better evaluation of the stimulation setting for the treatment optimization.

I. Introduction

Over the past decade increasing attention has been given to deep brain stimulation (DBS) because of its ability to recalibrate the activity of dysfunctional brain circuits through the electrical stimulation of selected targets inside the brain [1]. DBS of the subthalamic nucleus (STN) was shown to improve some of the symptoms of patients affected by advanced Parkinson's disease with inadequate response to drug therapy.

The precise mechanism of the therapeutic action of DBS is currently unclear, limiting the possibility to improve treatment efficacy and to simplify the post-operative management of the device. Great effort has been dedicated to investigating the variables influencing the outcome of the stimulation, including contact configurations, frequency, current steering, pulse width and voltage, and the electrode geometry [2]. Moreover, the stimulation also depends on the differing bioimpedance of the brain tissues surrounding the implant [3].

In this paper we present a computational head model to calculate the electric field distribution generated by DBS in the region surrounding the electrode. The spatial resolution used for the presented model (isotropic 0.5mm) and the high quality and contrast of the original image data allowed for a detailed anatomical characterization of the basal ganglia and the thalamic nuclei, which make it particularly suitable for applications involving DBS. Numerical simulations were performed to investigate the changes in the electric field generated by DBS with different configurations of bipolar stimulation.

II. Materials and Methods

A. Anatomical Model

Images of the head and neck at the level of the fifth cervical vertebra (C5) of one healthy 29-year old female volunteer were acquired on a PHILIPS Achieva 3 Tesla magnetic resonance imaging (MRI) scanner (Philips Healthcare, Best, The Netherlands) using an eight-channel receive head coil array. To obtain anatomical images with suitable contrast at a high resolution the following sequences were performed: *i)* 0.5mm isotropic resolution whole head T1-weighted three-dimensional (3D) magnetization prepared gradient echo and T2-weighted 3D turbo spin echo, *ii)* 0.5mm isotropic resolution T2-weighted turbo spin echo imaging slab to image the eyes and the ear regions with improved nerve contrast and *iii*) 3D time of flight ($0.39 \times 0.39 \times 0.5\text{mm}^3$ resolution) and 3D phase contrast angiography ($0.72 \times 0.72 \times 0.8\text{mm}^3$ resolution) optimized to distinguish arteries and veins respectively. Each dataset was resampled to a 0.5mm isotropic resolution and aligned to the reference T1-weighted MRI dataset using an affine registration based on normalized mutual information [4]. The segmentation process was performed using the iSeg software [5] with all the available datasets. For each structure, the general segmentation procedure was performed using multiple slices at a time with the first and last slices undergoing segmentation followed by interpolation of the

Research supported by U.S. Food and Drug Administration's Critical Path Initiative, CTI (14930.1 PFLS-LS) and in part by the Research Participation Program at the Center for Devices and Radiological Health administered by the Oak Ridge Institute for Science and Education through an interagency agreement between the U.S. Department of Energy and the U.S. Food and Drug Administration. The mention of commercial products, their sources, or their use in connection with material reported herein is not to be construed as either an actual or implied endorsement of such products by the Department of Health and Human Services.

M. I. Iacono, E. Akinnagbe, E. Cohen, W.Kainz, and L. M. Angelone are with Division of Physics, Office of Science and Engineering Laboratories, Center for Devices and Radiological Health, U.S. Food and Drug Administration, Silver Spring, MD. USA (e-mail: Maria.Iacono@fda.hhs.gov).

E. Neufeld and N. Kuster are with the Foundation for Research on Information Technologies in Society (IT'IS), 8004 Zurich, Switzerland.

A. Jakab is with Computational Image Analysis and Radiology Laboratory, Medical University of Vienna, 1090 Vienna, Austria. G. Bonmassar is with A. A. Martinos Center for Biomedical Imaging, Dept. of Radiology, MGH, Charlestown, MA, USA.

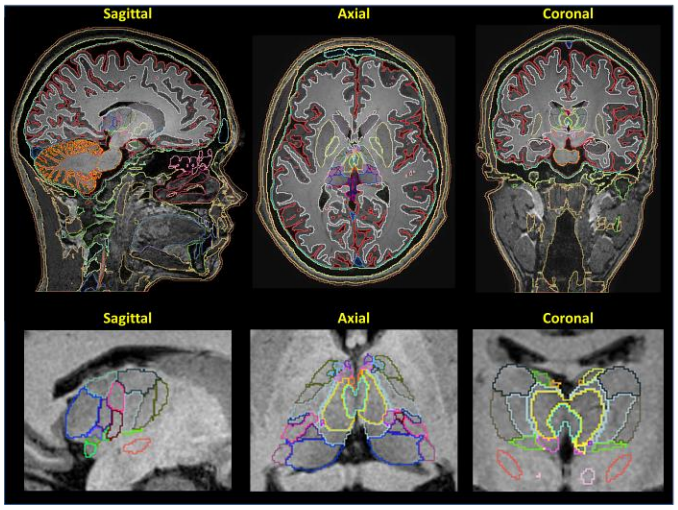

Fig. 1. (*top*) Results of segmentation of the head model in the sagittal, axial, and coronal views. (bottom) Magnified sagittal, axial, and coronal views of the thalamus. In each pair, the segmentation is shown on the MRIs as a color-coded label map.

TABLE I. LIST OF THE SEGMENTED NUCLEI IN THE MODEL

Nuclei	
Anterodorsal (AD)	Inferior Pulvinar (PuI)
Anteromedial (AM)	Lateral Pulvinar (PuL)
Anteroventral (AV)	Medial Pulvinar (PuM)
Central Lateral CL	Mammillothalamic tract (mtt)
Centromedian (CM)	Paraventricular (Pv)
Central Medial (CeM)	Red nucleus (RN)
Habenular (Hb)	Subparafascicular (sPf)
Lateral Dorsal (LD)	Suprageniculate (SG)
Lateral Geniculate magnocellular (LGNmc)	Subthalamic (STN)
Lateral Geniculate parvocellular (LGNpc)	Ventral Anterior magnocellular (VAmc)
Lateral posterior (LP)	Ventral Anterior parvocellular (VApc)
Limitans (Li)	Ventral Lateral Anterior (VLa)
Mediodorsal magnocellular (MDmc)	Ventral Lateral - Posterior Dorsal (VLpd)
Mediodorsal parvocellular (MDpc)	Ventral Lateral - Posterior Ventral (VLpv)
Medial geniculate (MGN)	Ventral Medial (VM)
Medioventral (MV)	Ventral Posterior Inferior (VPI)
Parafascicular (Pf)	Ventral Posterior Lateral -Anterior (VPLa)
Posterior (Po)	Ventral Posterior Lateral -Posterior (VPLp)
Anterior Pulvinar (PuA)	Ventral Posterior Medial (VPM)

slices in between and subsequent correction. Segmentation into 142 structures of the head and neck was complemented by extensive manual adjustment and smoothing and verified by an expert anatomist. Fig. 1 shows the final result of the segmentation (*top*) on a sagittal, axial and coronal MRI slice. A specific automatic atlas-based segmentation was dedicated to the segmentation of the thalamus and its nuclei. Ground truth data for the anatomy of thalamic nuclei were acquired from the 3D adaptation of a multi-architectonic stereotactic thalamus atlas by Morel [6]. We relied on the extension of the classical two-dimensional atlas with multi-subject data: multiple histological delineations were fused into a statistical shape model based digital atlas [7]. The histological procedure of the original atlas generation and anatomical nomenclature is detailed in [6, 7]. In these shape models, the mean geometry of the thalamic nuclei and their dimensional variability are shown

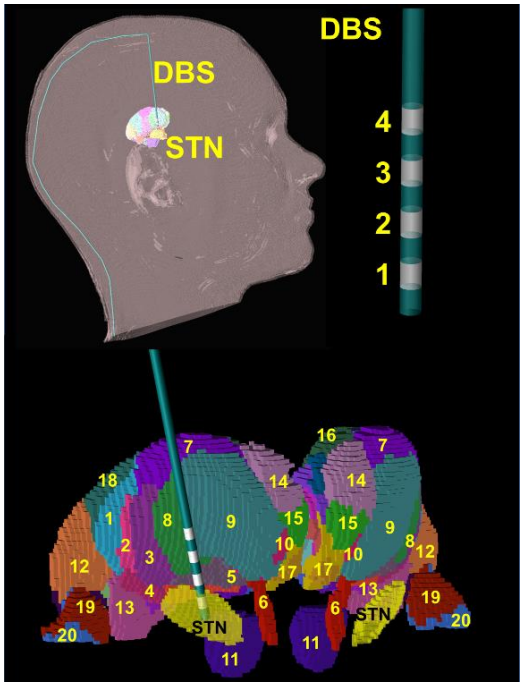

Fig 2. The head model with the implanted DBS electrode (top) and a magnified view of the thalamus with the electrode inserted in the STN (bottom). Legend of the segmented nuclei: 1 VPLp; 2 VPLa; 3 VLpv; 4 VPI; 5 VM; 6 mtt; 7 VLpd; 8 Vla; 9 Vapc; 10 Vamc; 11 RN; 12 PuL; 13 MGN; 14 AV; 15 AM; 16 LD; 17 CeM; 18 LP; 19 LGNpc; 20 LGNmc

and can be utilized to make predictions about an individual (subject-specific) anatomical configuration, which remains feasible when only partial observations are possible [8]. The procedure described in [9] was followed and the borders of the thalamus visible in the MRI were used to estimate a subject specific map of individual thalamus nuclei. For this step, manual segmentation of thalamus borders was performed on the T1-weighted MRI images. The resulting triangulated meshes of nuclei were projected onto the image grid of the original MRI acquisitions and volumetric representations were saved. At the bottom of Fig. 1, a magnified view of the thalamus is shown with the outlines of segmented nuclei overlaid. A list of the 38 thalamic nuclei included in the segmentation is provided in Table I.

B. Electrical Head Model

The anatomical model was converted into a bioelectric model by assigning electrical properties to each anatomical structure [10]. Commercially available software (SEMCAD low-frequency solver, Schmid & Partner Engineering AG, Zurich, Switzerland) was used for electric field simulations. A non-uniform electrical grid was used to discretize the domain: a 1mm isotropic grid for the head and a 200µm isotropic grid for the tip of the lead The electrical parameters were considered to be: 1) constant in frequency, 2) isotropic, and 3) heterogeneous in space.

C. Model of implant

One unilateral implant was modeled as an insulated lead with an array of four cylindrical electrode contacts at the distal tip [11]. The contacts were modeled as conductive cylindrical rings (1.5mm in height, 1.27mm in external diameter, 0.8mm

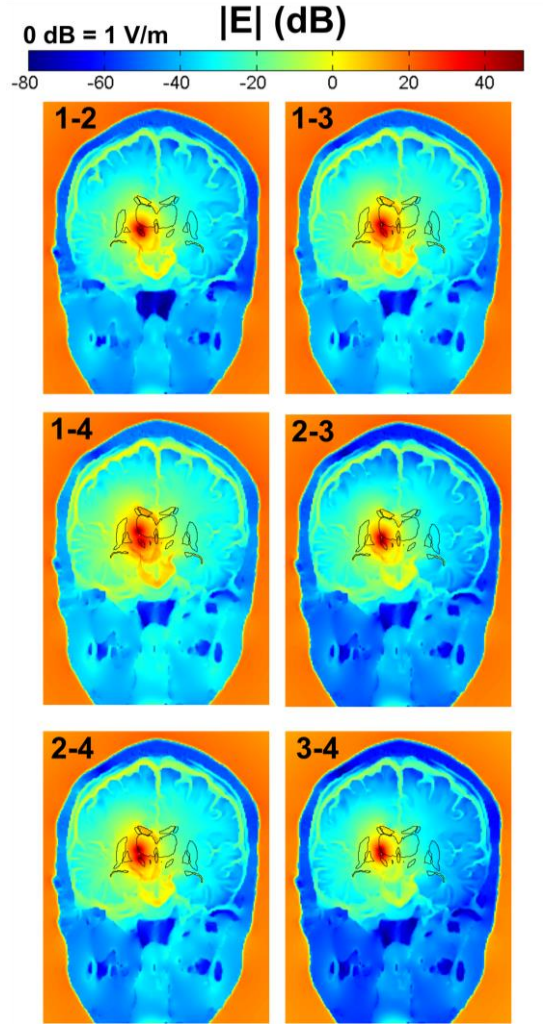

Fig. 3. Maps of the magnitude of electric field for the 6 different bipolar configurations. High values are visible near the electrode and in the CSF.

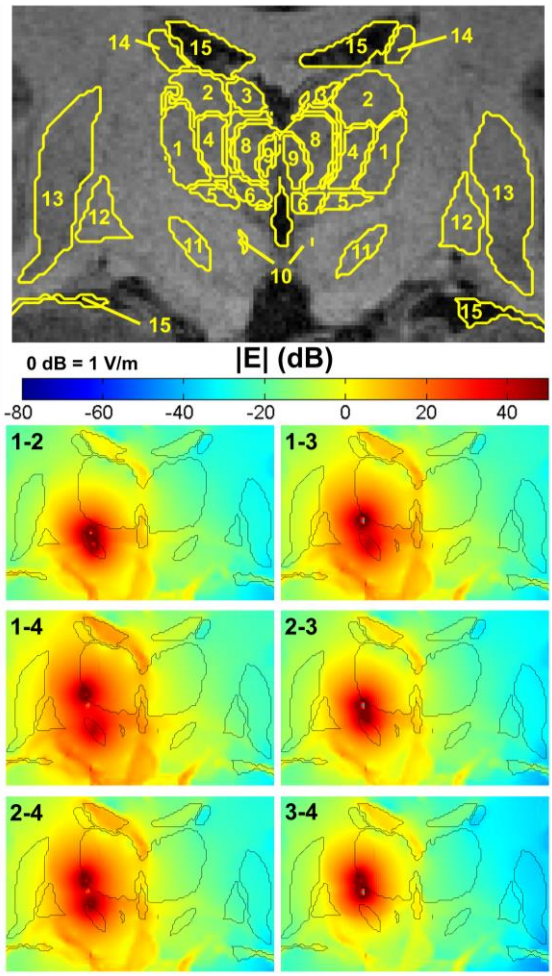

Fig. 4. (*Top*) coronal view of the thalamic nuclei on the T1-weighted MRI. Legend of the segmented nuclei: 1 Vla; 2 VLpd; 3 AV; 4 VLpv; 5 VM; 6 CeM; 7 CL; 8 MDpc; 9 MDmc; 10 mtt; 11 STN; 12 pallidum; 13 putamen; 14 caudate; 15 ventricles. (*Bottom*) Magnitude of electric field in the nuclei for the 6 bipolar configurations (1-2, 1-3, 1-4, 2-3, 2-4, 3-4).

internal diameter) separated by fully insulated cylinders (1.5mm in height, 1.27mm diameter) (Fig. 2). The conductive sections of the lead were modeled as a perfect electric conductor (PEC), whereas the electrical conductivity and permittivity of the insulated sections were $\sigma = 0$ S/m and $\varepsilon_r = 3$ respectively [12, 13]. The proximal end of the lead was in the neck of the head model, and the lead was placed along a unique sagittal plane in the subcutaneous structure between the epidermis and the outer table, penetrating coronally through the outer table along the brain up to the segmented STN [14]. A bipolar electrode configuration was implemented and each of the four contacts of the quadripolar DBS model was modeled as a cathode or anode for a total of 6 combinations: 1-2, 1-3, 1-4, 2-3, 2-4, 3-4. A sinusoid with amplitude of 1 V and frequency of 100 Hz was used to drive the stimulation. Fig. 2 shows the head model with the implanted DBS (*top*) and a magnified view of the thalamus and the electrode inserted in the STN (*bottom*).

D. Electromagnetic simulations

Under the assumption that the quasi-static regime applies [15], the electric field generated by DBS was calculated by solving the Laplace equation:

$$\nabla \cdot \sigma \nabla V = 0$$

where V is the potential (V), and σ is the electrical conductivity (S/m). For each bipolar configuration, the peak, the mean and the standard deviation of the intensity of the electric field in the STN (i.e., the intended target of the stimulation), in the thalamus, and in the pallidum were calculated.

III. Results

Fig. 3 and Fig. 4 show the magnitude of electric field over the head with the six different bipolar configurations. The outline of the anatomical structures surrounding the electrode is overlaid for visualization purposes. The absolute peak of intensity of the electric field was 854 V/m, 894 V/m, and 875 V/m for the three narrow bipolar configurations (1-2, 2-3, and 3-4, respectively), and 750 V/m, 619 V/m and 672 V/m for the wide configurations (1-3, 2-4, and 1-4, respectively). Table II reports the magnitude of electric field in the STN, thalamus and pallidum. The highest intensity of electric field

TABLE II. PEAK, MEAN AND STANDARD DEVIATION (SD) OF THE INTENSITY OF THE ELECTRIC FIELD IN STN, THALAMUS AND PALLIDUM

Bipolar Configurations	STN			Thalamus			Pallidum		
	Peak (V/m)	*Mean (mV/m)*	*SD (V/m)*	*Peak (V/m)*	*Mean (mV/m)*	*SD (V/m)*	*Peak (V/m)*	*Mean (mV/m)*	*SD (V/m)*
1-2	854	2.60	± 0.79	126	1.90	± 0.12	7	0.3	± 0.02
1-3	360	1.63	± 0.42	707	4.34	± 0.47	11	0.54	± 0.04
1-4	401	1.72	± 0.45	673	6.57	± 0.57	14	0.80	± 0.06
2-3	339	9.61	± 0.32	654	3.17	± 0.43	7	0.36	± 0.03
2-4	370	1.13	± 0.34	619	5.23	± 0.52	12	0.62	± 0.05
3-4	46	1.62	± 0.04	875	4.10	± 0.69	7	0.29	± 0.02

(854 V/m) in the STN was found for the configuration 1-2. This configuration maximized the field in the target, while minimizing it in the surrounding thalamus. Opposite results were obtained with the configuration 3-4, which generated a maximum electric field in the thalamus. All configurations generated a low intensity electric field in the pallidum.

IV. CONCLUSION

Accurate geometric modeling of the human brain anatomy combined with a correct electric characterization of the tissues bioimpedance allowed us to investigate the interactions between the DBS and the deep brain tissues. Diffusion tensor imaging data are available for this model and will be used in future studies to incorporate the tissues anisotropy [3]. The model did not include neural and fibers activation. However, it did allow calculation of a precise map of the electric field in the region of the electrode, which is closely related to the neural activation. The relation between neural activation and the second spatial derivative of the extracellular potential distribution ($\partial^2 V_e/\partial x^2$) is described by the Rattay activation function [16].

Future work may account for differences in tissue bioimpedance among the nuclei or for changes related to population variability (e.g., aging). Furthermore, a detailed uncertainty assessment will be performed, including the effect of spatial resolution and convergence analysis. Peak values of electric field magnitude are particularly sensitive to the applied discretization. The peaks of the electric field for the narrow bipolar configurations (1-2, 2-3, 3-4), where contacts are adjacent, were higher than those observed for the wide bipolar configurations, where the anode and cathode are separated by one or two unused contacts. The narrow bipolar configurations provided the smallest volume of electric fields, but the highest intensity, compared with the wide configurations. Increased distance causes in turn increased resistance and reduces the overlap of high fields in the electrode vicinity, with the result that narrow configurations focused the electric field locally, while wide configurations spread the field out in the surrounding regions. The therapeutic efficacy is primarily related to the location of the stimulation. Reduced efficacy and side-effects may be caused by unintentionally stimulating undesired regions and, as a consequence, precise targeting is critical to achieve the desired efficacy [17]. The considerations regarding the shape, size and intensity generated by different electrode configurations suggested by the proposed model could be exploited for an effective and efficient postoperative DBS programming to steer the current toward the target, maximize the efficacy, and minimize the side effects due to the unintended stimulation.

ACKNOWLEDGMENT

The authors thank J. Wolf for her scientific support.

REFERENCES

[1] J. S. Perlmutter and J. W. Mink, "Deep brain stimulation," *Annu Rev Neurosci,* vol. 29, pp. 229-57, 2006.

[2] A. M. Kuncel and W. M. Grill, "Selection of stimulus parameters for deep brain stimulation," *Clin Neurophysiol,* vol. 115, pp. 2431-41, 2004.

[3] C. C. McIntyre, S. Mori, D. L. Sherman, N. V. Thakor, and J. L. Vitek, "Electric field and stimulating influence generated by deep brain stimulation of the subthalamic nucleus," *Clin Neurophysiol,* vol. 115, pp. 589-95, Mar 2004.

[4] P. Viola and W. M. Wells III, "Alignment by maximization of mutual information," *Int journal of computer vision,* vol. 24, pp. 137-154, 1997.

[5] E. Neufeld, "High resolution hyperthermia treatment planning," PhD, Swiss Federal Institute of Technology, Zurich 2008.

[6] A. Morel, *Stereotactic atlas of the human thalamus and basal ganglia*: CRC Press, 2007.

[7] A. Krauth, R. Blanc, A. Poveda, D. Jeanmonod, A. Morel, and G. Székely, "A mean three-dimensional atlas of the human thalamus: generation from multiple histological data," *Neuroimage,* vol. 49, pp. 2053-2062, 2010.

[8] A. Rao, P. Aljabar, and D. Rueckert, "Hierarchical statistical shape analysis and prediction of sub-cortical brain structures," *Medical image analysis,* vol. 12, pp. 55-68, 2008.

[9] A. Jakab, R. Blanc, E. Berényi, and G. Székely, "Generation of Individualized Thalamus Target Maps by Using Statistical Shape Models and Thalamocortical Tractography," *American Journal of Neuroradiology,* vol. 33, pp. 2110-2116, 2012.

[10] C. Gabriel, S. Gabriel, and E. Corthout, "The dielectric properties of biological tissues: III. Parametric models for the dielectric spectrum of tissues," *Phys. Med. Biol.,* vol. 41, pp. 2271–2293, 1996.

[11] M. I. Iacono, N. Makris, L. Mainardi, L. M. Angelone, and G. Bonmassar, "MRI-Based Multiscale Model for Electromagnetic Analysis in the Human Head with Implanted DBS," *Computational and Mathematical Methods in Medicine,* vol. 2013, p. 12, 2013.

[12] A. Taflove and K. R. Umashankar, "The Finite-Difference Time-Domain Method for Numerical Modeling of Electromagnetic-Wave Interactions," *Electromagnetics,* vol. 10, pp. 105-126, Jan-Jun 1990.

[13] S. A. Mohsin, N. M. Sheikh, and U. Saeed, "MRI-induced heating of deep brain stimulation leads," *Phys Med Biol,* vol. 53, pp. 5745-56, 2008.

[14] N. Makris, L. Angelone, S. Tulloch, S. Sorg, J. Kaiser, D. Kennedy, *et al.*, "MRI-based anatomical model of the human head for specific absorption rate mapping," *Med Biol Eng Comput,* vol. 46, pp. 1239-51, Dec 2008.

[15] R. Plonsey and D. B. Heppner, "Considerations of quasi-stationarity in electrophysiological systems," *Bull Math Biophys,* vol. 29, pp. 657-664, 1967.

[16] F. Rattay, "Analysis of models for external stimulation of axons," *Biomedical Engineering, IEEE Transactions on,* pp. 974-977, 1986.

[17] E. B. Montgomery, Jr. and J. T. Gale, "Mechanisms of action of deep brain stimulation(DBS)," *Neurosci Biobehav Rev,* vol. 32, pp. 388-407, 2008.